Prediction of resistance reduction for ice-going ships installed with air-bubbling systems

Downloaded from: https://research.chalmers.se, 2025-04-24 03:00 UTC

Citation for the original published paper (version of record):

Wei, H., Ni, B., Li, Z. (2025). Prediction of resistance reduction for ice-going ships installed with air-bubbling systems. Cold Regions Science and Technology, 236.
http://dx.doi.org/10.1016/j.coldregions.2025.104509

N.B. When citing this work, cite the original published paper.

research.chalmers.se offers the possibility of retrieving research publications produced at Chalmers University of Technology. It covers all kind of research output: articles, dissertations, conference papers, reports etc. since 2004. research.chalmers.se is administrated and maintained by Chalmers Library

(article starts on next page)

Cold Regions Science and Technology 236 (2025) 104509

Contents lists available at ScienceDirect

Cold Regions Science and Technology

journal homepage: www.elsevier.com/locate/coldregions

Prediction of resistance reduction for ice-going ships installed with air-bubbling systems

Hongyu Wei [a], Baoyu Ni [a,*], Zhiyuan Li [b,*]

[a] College of Shipbuilding Engineering, Harbin Engineering University, Harbin 150001, China
[b] Department of Mechanics and Maritime Sciences, Chalmers University of Technology, Gothenburg, Sweden

ARTICLE INFO

Keywords:
Ice-going ship
Air-bubbling system
Model test
Numerical simulation
Ice resistance

ABSTRACT

To investigate the drag reduction mechanism and variation in the efficiency of the air-bubbling system, we designed and conducted model ship experiments under an ice floe channel using a self-designed navigation device, force measurement system, camera observation system, and prototype of an air-bubbling system, based on a polypropylene non-refrigerated model ice. During the experiments, the navigation device allowed the ship to pitch, roll, and heave, while adjusting the air-bubbling system's gas flow rate, ship speed, and ice concentration to explore factors affecting the efficiency of the air-bubbling system. Building upon the model ship experiments, we further explored the drag reduction mechanism and effects of the air-bubbling system through coupled CFD-DEM numerical simulations. The research findings indicate that the drag reduction rate of the air-bubbling system decreases approximately linearly with increasing ice concentration and ship speed. Conversely, increasing the gas flow rate synchronously increases the drag reduction effect, albeit with a more pronounced marginal utility. Additionally, we conducted numerical calculations on the drag reduction rates of two additional ship types equipped with the air-bubbling system. Using multi-parameter linear fitting, we derived an empirical formula for estimating the drag reduction rate of the air-bubbling system under different conditions.

1. Introduction

Vessels that navigate ice regions can be divided into icebreakers and ice-going ships based on their icebreaking capabilities and purposes. Icebreakers are featured by special bow and hull shapes and more powerful propulsion systems, allowing them to break through level ice (Ni et al., 2020a). Ice-going ships, in contrast, have normal hull shapes and limited ice navigation capabilities, which implies they can navigate independently in marginal ice zones but need icebreaker assistance in severe ice conditions. Auxiliary icebreaking systems can enhance the ice navigation capabilities of ice-going ships. Among the existing auxiliary icebreaking systems, air-bubbling systems have been successfully installed in icebreakers in the United States, Canada, and Russia (Sodhi et al., 1995).

The air-bubbling system studied in this paper shares some similarities with the air lubrication system, which has been utilized for the reduction of resistance for ships navigating in open water. The underlying theories for bubble-induced resistance reduction have been developed by researchers such as McCormick et al. (2010), which can be categorized into bubble-induced skin-friction drag reduction (BDR) (Wang et al., 2004), and air layer drag reduction (ALDR) (Wang et al., 2011). Elbing et al. (2013) conducted experiments to study the relationship between these two types of drag reduction and their mechanism transitions. It is noteworthy that the air lubrication system requires a stable presence of microbubbles or an air layer on the hull to reduce friction between the hull and the surrounding fluid. In contrast, this work's air-bubbling system generates a gas-liquid mixture from bubbles rising to the water surface, thereby reducing ship-ice contact and lowering the ship's ice resistance.

The mechanism of how the air-bubbling system reduces ice resistance has not been fully understood. Research on air-bubbling systems started from full-scale tests. The first reported air-bubbling system was first installed on a Ro-Ro ship operated in the Baltic Sea as early as 1969 (Juurmaa et al., 1978). Extensive development and testing of the system have been used in several vessels till the early 1990s (Wilkman et al., 2011). However, no theoretical or numerical studies on the mechanism of how the air-bubbling system reduces ice resistance have been reported until recent years. Ni et al. (2020b) conducted model-scale experiments to preliminarily explore the principles of the air-bubbling system in freshwater ice, observing cavity formation by bubbles under

---

* Corresponding authors.
E-mail addresses: nibaoyu@hrbeu.edu.cn (B. Ni), zhiyuan@chalmers.se (Z. Li).

https://doi.org/10.1016/j.coldregions.2025.104509
Received 3 September 2024; Received in revised form 7 February 2025; Accepted 28 March 2025
Available online 29 March 2025
0165-232X/© 2025 The Authors. Published by Elsevier B.V. This is an open access article under the CC BY license (http://creativecommons.org/licenses/by/4.0/).

the ice. Ni et al. (2021) conducted tests in an ice floe channel with a ship model installed with the air-buddling system. Ice-free zones were observed on the water surface close to the ship's sides when the air-bubbling system was activated. Based on these studies, Guo (2021) conducted numerical simulations to investigate the resistance reduction efficiency of the air-bubbling system by studying water and ice flowing past a stationary ship model at a certain speed. It was found that the air-bubbling system was more effective in reducing contact between the ship's sides and ice. Further, Ni et al. (2022) built CFD-DEM coupled models to numerically investigate the resistance reduction effects of the air-bubbling system at different jet speeds from the bow and side nozzles.

The above-mentioned experimental and numerical studies provided insights on the principles of air-bubbling systems. However, in the previous studies were carried out on a stationary hull with a flow field and floating ice moving past at a certain speed, which failed to provide a quantitative description of the drag-reduction efficiency of the air-bubbling system or to reveal the underlying reasons for the influence of different factors on this efficiency. This paper, in contrast, focuses on the drag-reduction mechanism of air-bubbling systems, aiming to find out the effects of various factors, such as different ship speeds, air injection rates, and ice concentration, on the drag-reduction efficiency of the air-bubbling system through more refined model tests and numerical simulations that match the experimental conditions without simplification. Furthermore, using validated numerical models, the drag-reduction efficiency of air-bubbling systems for different ship types was determined through numerical simulations. Using multi-parameter linear fitting, an empirical formula for quickly estimating the drag-reduction efficiency of bubble systems was finally derived.

2. The experimental setup

The experiments were conducted in an outdoor ice-water tank, with tank dimensions of 20 m × 2 m × 1.5 m. The main dimensions of the experimental ship model are presented in Table 1. Experience from ship model tests indicated that the influence of the tank boundaries could be neglected when the tank width exceeded five times that of the ship model. Some references have discussed the influence of channel width on the ice resistance, such as Yang et al. (2024). During the experiments, we designated a test section of 10 m × 2 m to provide sufficient length for the acceleration, deceleration, and open-water navigation of the ship model. During the experiments, the freedoms of movement for pitch, roll, and heave are allowed, which is recommended by Huang et al. (2018) and Zong et al. (2020).

The experiments were conducted using non-refrigerated ice. Non-refrigerated model ice has been widely utilized to simulate ice without secondary breakup. Corlett et al. (1964) were the first reported to use paraffin material to prepare non-refrigerated model ice to agreeable results. Since then, various materials have been used to make non-refrigerated model ice for studies on ship model ice resistance. Bergsma et al. (2014) used polypropylene model ice for experiments, with results that were consistent with empirical formulas. Kim et al. (2009) found through experiments that the results of ship model ice resistance using non-refrigerated model ice were in good agreement with those using frozen model ice. Because the objective of this work is on the drag reduction effect of the air-bubbling system in channels with small floating ice blocks, the movement of small floating ice is simplified as rigid body motion, while the fragmentation and bending of sea ice are not considered. The model ice used in the experiments was made of polypropylene (PP) material, with a density similar to that of sea ice (the density of PP is 860-920 kg/m^3, the density of ice is 880-930 kg/m^3) and a friction coefficient close to that of sea ice. The measured kinetic friction coefficient in the experiments is shown in Table 2.

Table 1
Main dimensions of actual ship and ship model.

	Full-scale	Model-scale (λ = 60)
Length overall (m)	122.5	2.04
Breadth (m)	22.3	0.37
Draught (m)	7.9	0.13

To prevent bending or fracturing, it is necessary to restrict the size of the ice blocks. According to the Mindlin plate theory based on elasticity, the fracture of ice blocks can be neglected when their size is smaller than the typical lengths mentioned below (Kim et al., 2015; Lu et al., 2016).

$$l = \sqrt[4]{\frac{D}{k}} \tag{1}$$

where D represents the flexural rigidity of ice, expressed as:

$$D = \frac{Et^3}{12(1 - \upsilon^3)} \tag{2}$$

where E represents Young's modulus, v represents the Poisson's ratio, t represents the ice thickness, and k represents the elasticity coefficient, with a value of ρg, where ρ is the density of water and g is the acceleration due to gravity.

The water surface is typically covered by a field of ice floes, for which the shape, size, and thickness may vary randomly. However, for simplicity, the ice thickness in this work is assumed to be 1.67 cm (equivalent to 1 m in full-scale). The Young's modulus is set to 16.67 MPa (corresponding to 1 GPa for real-scale ice) (Timco et al., 1984). Based on this standardization, we calculate the maximum size of floating ice blocks using typical length formulas, resulting in an approximate size of 16.14 cm. Similarly, the ice floe shape in this study is assumed as square-shaped 6.7 cm × 6.7 cm, which implies the full-scale ice floe has a dimension of 4 m × 4 m × 1 m. However, ships in actual navigation face complex sea ice environments, where ice failure, fracturing, and other phenomena may occur during ship-ice interactions. Nevertheless, such situations are not considered in this study. Besides, the ice floes are assumed to be evenly distributed across the surface of the test section, as depicted in Fig. 1:

The experiments are composed of 36 conditions in total. A condition is a combination of the ice concentration, the ship speed, and the gas flow rate. The ice concentration is set at 40 %, 60 %, and 80 %; the towing speed is set at 0.5 m/s, 0.6 m/s, and 0.7 m/s, while the gas flow rate is set at 0, 25, 35, and 45 L/min (Wilkman et al., 2011). To ensure an ample amount of data for analyzing the uncertainties of the experiments, each condition is replicated three times. Following each towing session, the range of the ice floe field is manually adjusted to guarantee that the length of each ice channel adheres to the experimental requirements and to attain as uniform a distribution of ice as feasible.

Ensuring geometric and hydrodynamic similarity criteria is crucial when conducting ship model tests in ice floe areas. In terms of hydrodynamics, maintaining equal Froude numbers and inducing bow waves are necessary to minimize the influence of model ship bow wave-induced resistance. Given that the experiment utilizes non-fragmentable polypropylene model ice, only geometric similarity can be guaranteed for the model ice. However, in this experiment, due to the presence of the air-bubbling system, the similarity of the gas flow rate also needs to be addressed. Currently, researchers mostly ensure the similarity of jetting velocity by matching Froude numbers (Song et al.,

Table 2
Comparison of friction coefficients.

Material	Kinetic friction coefficient	References
PP-ship model	0.19–0.27	Measured values
PP-PP	0.20–0.29	Measured values
Ice-ice	0.19–0.47	Erland et al. (2012)
Ice-steel (corroded)	0.14–0.40	Timco et al. (2010) Woolgar et al. (2010)
Ice-steel (painted)	0.04–0.20	Frederking et al. (2002)

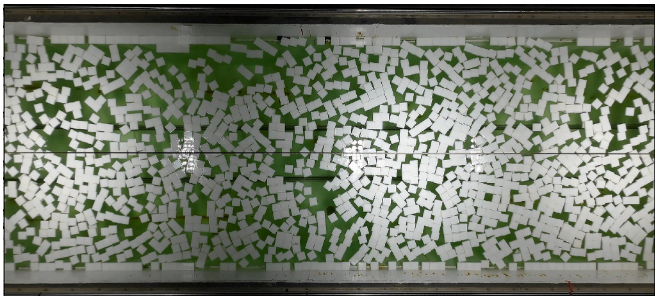

Fig. 1. Ice floe field during the experimental process.

2019). Considering the geometric similarity of the jet nozzle itself, the conversion of the gas flow rate satisfies a relationship proportional to the scale factor λ raised to the power of 2.5.

The experiments are conducted through ship model towing. The towing system mainly consists of a towing carriage, guide rail, motor, control box, steel cable, and limit switch. The towing carriage is driven by traction from the steel cable, and the towing speed can be adjusted within the range of 0 to 2 m/s with an adjustment precision of up to 0.001 m/s. During the experiment, the ship model is connected to the towing carriage through a navigation device. The navigation device is fixed on the towing carriage using a threaded clamp, with a tension and compression sensor connected to its lower end. This sensor is linked to a fixed device at the midpoint of the ship model's center of gravity, allowing for the measurement of the ship's towing resistance. Additionally, a limit sliding rail is installed at the rear of the ship model to ensure its straight-line motion. The sensor has a range of 100 kg, Ingress Protection (IP68) waterproof rating, precision of 0.03 % Full scale, and operates within a temperature range of −40 °C to 60 °C. In addition to the force measuring device, cameras synchronized with the towing carriage are used to record experimental phenomena. Ingress Protection Two camera positions are set up at the bow and side of the ship. The air-bubbling system consists of an air pump, pressure stabilizing chamber, manifold, and nozzles. The air volume can be adjusted by regulating the air pump. The ship model has openings in the hull, with eight jet orifices on each side. The schematic of the ship model connection and the ship model openings are illustrated in Fig. 2:

For the air-bubbling system in this study, as shown in Fig. 3, eight nozzles are placed on each side of the ship. The diameter of each nozzle is 6 mm, and the nozzles are symmetrically distributed along the ship's longitudinal plane. The nozzles are located 0.5 times the draft below the waterline, with a spacing of approximately 1 times the draft. The opening positions on the ship model and in the numerical simulation are consistent. During the experiment, an air compressor is used to supply air, which is distributed to each hole through a pressure-stabilizing device. The gas flow rate is adjusted by controlling the power of the air compressor.

3. Analysis of experimental results

3.1. Verification of experimental results

The ship resistance time history curves collected during the experiment can be divided into five parts: (1) the stationary stage before towing; (2) the acceleration stage of the ship model; (3) the open-water stage; (4) the ice floe stage; and (5) the deceleration stage. The typical time history curves of ship resistance and stage division are shown in Fig. 4. In the experiment described in this paper, conducted in an outdoor water tank, the presence of wind causes some oscillation in the zero-point collected during the stationary stage. Additionally, it is important to note that during the experiment, the air-bubbling system was already activated during the stationary stage. Therefore, the presence of the open water stage allows us to measure the impact of the air-bubbling system on the ship's water resistance, and provides validation for the numerical simulation method.

Considering the extraction of ice resistance, we assume that the total resistance consists of the linear superposition of water resistance and ice resistance. Therefore, the ice resistance of the ship model for each set of conditions can be obtained by subtracting the resistance during the open-water stage from the resistance during the ice floe navigation stage. A set of typical conditions (60 % ice concentration, 0.5 m/s velocity) was selected for comparison. The resistance in the open-water stage was 0.535 N, while the resistance in the ice floe stage was 2.125 N. The water resistance accounted for approximately 25 % of the total resistance of the ship under experimental conditions. Using the above assumptions, the ice resistance at this point can be calculated as 1.59 N. The specific open-water resistance results, along with further comparisons of experimental and numerical results, can be found in Table 5 in the following chapters.

The above experimental processing method carries certain risks. Specifically, the short navigation time during the open-water stage may introduce errors in the open-water resistance measurement. Therefore, each set of experimental conditions was repeated three times to ensure the consistency of the ship model test results under the experimental conditions and data processing methods outlined in this paper, as depicted in Fig. 5. In the figure, the error bars indicate the maximum and minimum resistance values of each condition set, while the data points represent the average of the three repeated tests for each condition set. The percentage below each set of data represents the reduction rate of ice resistance achieved by the air-bubbling system. It is noticeable that under low ice concentration conditions, the experimental results without jetting exhibit significant fluctuations. This is primarily due to the challenge of evenly distributing ice floe under such conditions. However, even in cases with the largest fluctuations, the range remains within 15 %. This underscores the validity of the experimental design and data processing methods employed in this study. In Fig. 5, the percentage below each data point represents the ice resistance reduction rate due to the air-bubbling system. This rate refers to the ratio of the reduction in ice resistance after activating the air-bubbling system to the

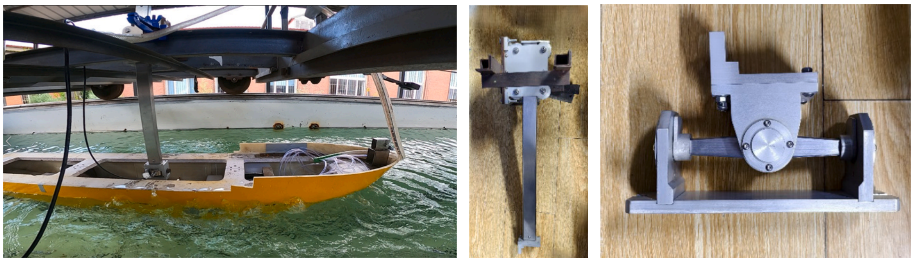

(a) (b) (c)

Fig. 2. Experimental Connection Device: (a) complete connection diagram; (b) the connecting rod responsible for the heaving function; (c) the connection base capable of both rolling and pitching.

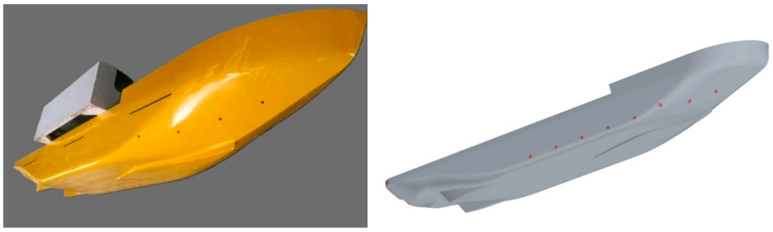

(a) Schematic of nozzle positions on the ship model (b) Schematic of nozzle positions in numerical simulation

Fig. 3. Schematic of the air-bubbling system opening positions in the experiment and numerical simulation.

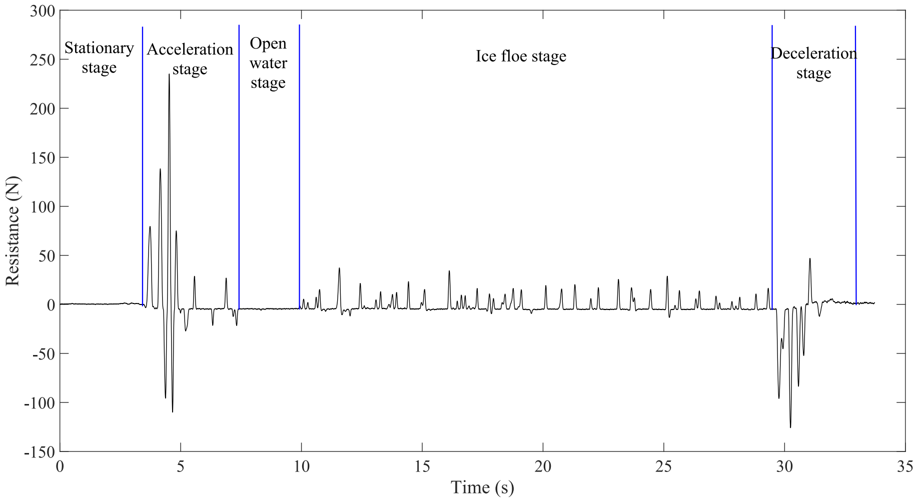

Fig. 4. Typical resistance time history curves of ship model experiment.

ice resistance when the bubble system is not activated.

3.2. *Analysis of factors influencing the drag reduction effect of the air-bubbling system*

Fig. 5 illustrates the curve of ice resistance under different ice concentrations as the gas flow rate varies. We can intuitively observe that as the gas flow rate increases, the ice resistance of the ship model continuously decreases. This phenomenon is straightforward to understand: with the increase in gas flow rate, the kinetic energy of the gas ejected from the nozzle also increases. This generates larger gas-liquid pulsations at the free liquid surface, creating stronger repulsion forces against the ice floe around the ship, consequently causing more ice floe to detach from the ship's hull, thereby reducing the ice resistance of the vessel.

Furthermore, by observing the change in resistance slope at different gas flow rates, we can notice that as the gas flow rate increases, the rate of decrease in ice resistance slows down. This can be easily explained: only the ice floe around the ship can exert an effect on the ship's hull. As the gas flow rate increases, more ice floe around the ship is pushed away from the hull. When the gas flow rate reaches a critical point, all ice floe around the ship is pushed away, and further increasing the gas flow rate cannot continue to reduce the ice resistance.

Of course, in reality, it is neither feasible nor economical to infinitely increase the gas flow rate to minimize ice resistance. Therefore, the ice resistance obtained from our experiments continuously decreases with the increase in gas flow rate and gradually approaches a theoretical minimum ice resistance.

Moreover, compared to higher concentrations, this deceleration trend is more pronounced under the 40 % concentration. This could be attributed to the lower concentration, where the distribution of ice floe is sparse, making it less likely for the ice floe around the ship to be constrained by the outer ice floe and more likely to be blown away from the ship. As shown in Fig. 6 (a), at a 40 % concentration, ice floe around the ship can be blown away from the hull to a greater distance. In Fig. 6 (b), at a 60 % concentration, the ice floe around the ship is limited in movement by the denser outer ice floe during the process of being blown away, making it difficult for the ice floe around the ship to be blown too far away and still prone to contact with the hull. As indicated by the red box in Fig. 6 (b), the ice floe at the ship's shoulder cannot be pushed away due to the force chain phenomenon of the outer ice floe. The situation at an 80 % concentration is similar to that at a 60 % concentration, but the phenomenon of limited movement of the ice floe away from the hull due to the mutual influence of the ice floe around the ship is more pronounced, which is also why the reduction rate under the same gas flow rate decreases continuously with the increase in concentration.

The impact of ice concentration can also be observed in the comparison of the wake width before and after activating the air-bubbling system, as shown in Fig. 7. As the concentration increases, the available space for movement between the ice floe decreases, resulting in a significant reduction in the wake width after activating the air-bubbling system.

In addition to the two influencing factors of the gas flow rate of the air-bubbling system and the concentration of ice in the channel, the towing speed of the ship model is also an important factor affecting the effectiveness of reducing ice resistance by the air-bubbling system. From Fig. 5, it can be observed that even at the same gas flow rate and ice concentration, the efficiency of ice resistance reduction by the air-bubbling system decreases continuously with increasing towing speed. The reason for this phenomenon may be the drag effect of water flow on gas, causing the position of gas to rise to the water surface and be dragged backward. As towing speed increases, the position of gas rising

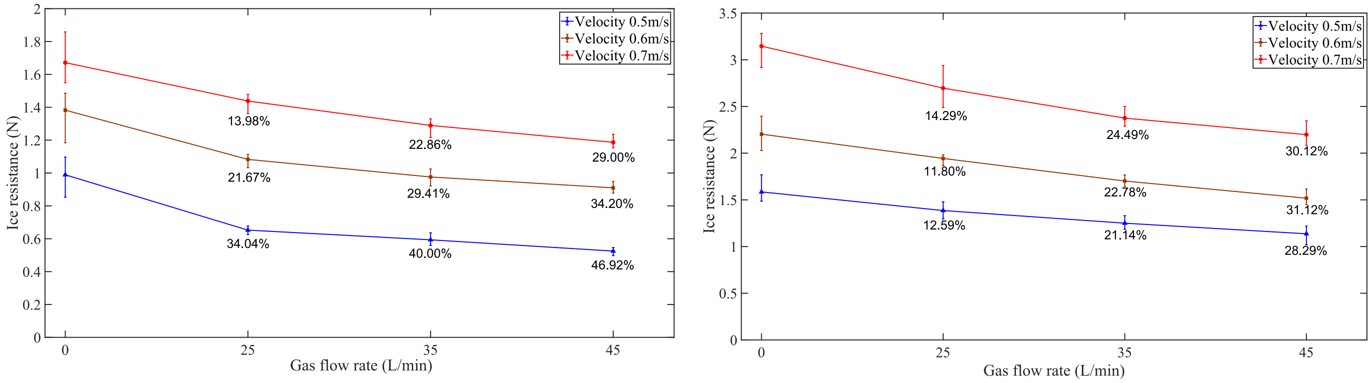

(a) 40% ice concentration

(b) 60% ice concentration

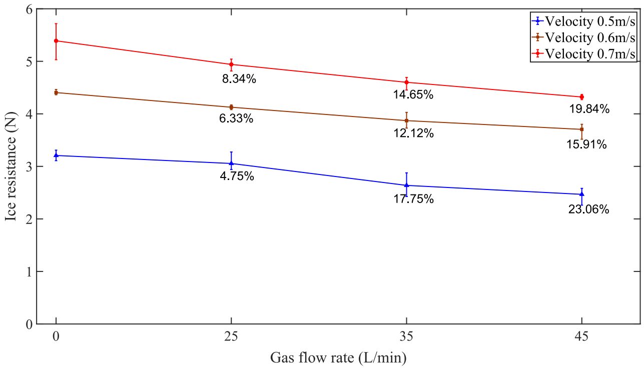

(c) 80% ice concentration

Fig. 5. Summary of experimental results (Different colors in the figure are used to distinguish the ship speeds, and the percentage below each data point represents the ice resistance reduction rate.)

(a) 40% ice concentration

(b) 60% ice concentration

Fig. 6. Ice movement around the ship after activating the air-bubbling system at different ice concentrations.

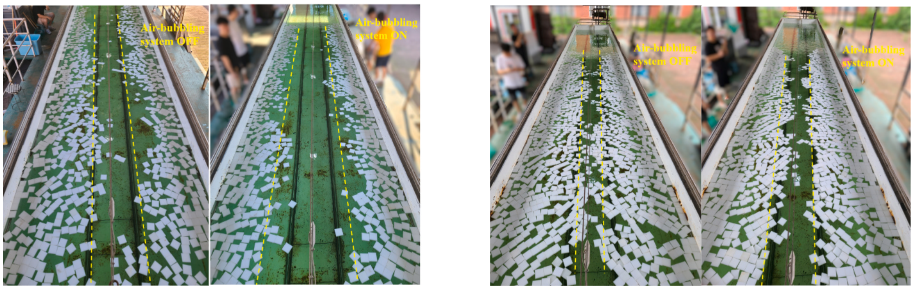

(a) 40% ice concentration

(b) 60% ice concentration

Fig. 7. The wake width changes after ship navigation under different ice concentration.

to the water surface is continuously delayed, resulting in a delayed action range of the air-bubbling system and an increase in the contact area between the ship and ice, thereby reducing the efficiency of ice resistance reduction. As indicated by the indicator line in Fig. 8, when the towing speed increases from 0.5 m/s in Fig. 8(a) to 0.7 m/s in Fig. 8(b), the starting position of the turbulent zone formed by gas on the

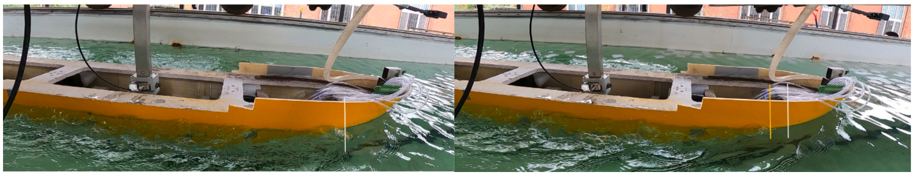

(a) towing speed 0.5m/s (b) towing speed 0.7m/s

Fig. 8. The starting position of the turbulent zone at different towing speed.

water surface moves significantly backward, shifting from the white indicator line to the yellow indicator line. However, the decrease in ice resistance reduction efficiency caused by the increase in towing speed under 60 % and 80 % ice concentrations in Fig. 5 is not significant compared to the 40 % ice concentration condition. The reason may be similar to the effect of ice concentration discussed earlier, that is, the increase in concentration makes it more difficult to blow ice floe away from the ship's hull. In this case, the degree of influence of the distance moved by gas due to drag toward the rear of the ship on the overall efficiency of ice resistance reduction is significantly weakened. Furthermore, the leading edge of the jetting-assisted icebreaking system itself is at the critical position where it begins to affect the ice floe. At this point, if the concentration is high, it becomes more difficult to push the ice floe away. Therefore, in conditions with higher concentrations, the effect of increasing speed on the efficiency of ice resistance reduction is weakened.

4. Comparison and analysis of numerical simulation results

The numerical simulation conditions are set the same as those in the model ship tests, and the numerical model is built strictly according to the test conditions. During the model ship tests, it is observed that the air-bubbling system generates strong flow field disturbances around the ship, and the flow field structure itself is highly complex. Additionally, considering the interaction between ice, the ship, water, and air, a numerical simulation based on a CFD-DEM coupled model is conducted. In the CFD-DEM coupled framework, the fluid phase is considered continuous, described by the Navier-Stokes Eqs. (N-S equations), while the solid phase is discrete, following Newton's and Euler's second laws. The two phases exchange data within a time step. The fluid phase parameters include velocity, pressure, temperature, and volume fraction, while the granular phase parameters include contact time, position, velocity, pressure, and intergranular interaction forces. In this study, the fluid phase comprises water and air, with an interface and interaction between them, representing a free surface flow problem of an incompressible viscous fluid. The solid phase consists of ice blocks, constructed using Discrete Element Method (DEM) particle units.

The coupling of CFD-DEM can be classified into one-way coupling and two-way coupling. In one-way coupling, only the forces exerted by the fluid phase on the granular phase are considered, without taking into account the influence of granules on the fluid. In two-way coupling, both the effect of the fluid on the granules and the effect of granular motion on the fluid are considered. Two-way coupling undoubtedly better reflects the actual physical processes. However, due to its significant computational resource consumption and limitations in handling a large number of complex interfaces, this study adopts a one-way coupling of CFD-DEM for numerical simulation research, given the focus on the impact of the air-bubbling system on ice floe.

4.1. Numerical model

In this study, the approach proposed by Zhong et al. (2023) has been adopted, where DEM particles are grouped into four batches and injected sequentially to enhance computational efficiency. Additionally, to ensure that DEM particles can be ejected normally under high concentration, DEM particles are arranged in a regular layout to construct the ice floe field. The ice floe model in this study is based on the DEM method, and its mechanical parameters are consistent with experimental values. The density of the ice floe is set to 920 kg/m^3, and the ship-ice friction coefficient is consistent with the measured value of 0.27 in this experiment. The Young's modulus of actual sea ice is taken as 1 GPa, and according to Cauchy number similarity (Timco et al., 1984), the Young's modulus in the numerical simulation is set to 16.67 MPa. The Poisson's ratio of sea ice in the numerical simulation is set to 0.3 (Vroegrijk et al., 2015). Since the experiment was conducted with fresh water, the density of water in the numerical simulation is set to 997 kg/m^3, and the density of air is set to the density at 25 °C atmospheric pressure, which is 1.18 kg/m^3.

The ship model and computational domain settings in the numerical model are identical to the model ship test conditions. In the numerical simulation, the right boundary is set as a velocity inlet condition, and the left boundary is set as a pressure outlet condition. The other boundaries in the background region use velocity inlet conditions. The ship surface uses a non-slip wall condition, and the free surface of the water is constructed using the VOF (Volume of Fluid) method. Contact models are set for DEM phase-DEM phase, DEM phase-VOF phase, and DEM phase-Wall interactions, as shown in Fig. 9, and the overlapping grid method is used to achieve data interaction during the ship's motion. The numerical model takes the endpoint of the stern as the coordinate origin, with the x-axis positive direction along the stern-to-bow direction, the y-axis positive direction along the port side, and the z-axis positive direction vertically upward. The overall size of the computational domain is the same as the size of the water tank in the model ship test, and the ice floe range in the numerical simulation is also a 10 m × 2 m area. Based on the physical background of the experimental conditions, the left boundary is set as a pressure outlet, the right boundary is a velocity inlet with the property of no penetration to prevent ice floe from escaping the computational domain, and the remaining boundaries are set as walls. The computational domain and ship model are divided using cut-cell meshing, with boundary layer grids added around the ship to ensure the y + values are within the range of 30–60, meeting the requirements of the K-Epsilon turbulence model. Additionally, the grid around the free surface is refined to ensure the accuracy of capturing the gas-liquid interface. There are also requirements for grid refinement at the nozzle, where according to Ni's specifications (2022), the nozzle should have at least 25+ complete grids to ensure that the jet flow does not experience significant numerical decay, as shown in Fig. 10. The total number of grid cells in the computational domain is approximately 2.49 million.

Similar to the experiments, the initial conditions for numerical simulations are set as calm water, no wind, and ice floe blocks statically floating on the water surface. After 0.2 s, the ship model starts to navigate at the prescribed speed to reduce initial numerical oscillations. Taking 60 % concentration as an example, the computational domain when the vessel enters the ice floe area is illustrated in Fig. 11:

In this study, Computational Fluid Dynamics (CFD) adopts the Finite Volume Method (FVM) for the numerical discretization of the fluid phase. It satisfies the fundamental equations of mass conservation and momentum conservation. Since the thermodynamic processes are not considered in this simulation, the energy conservation equation is not

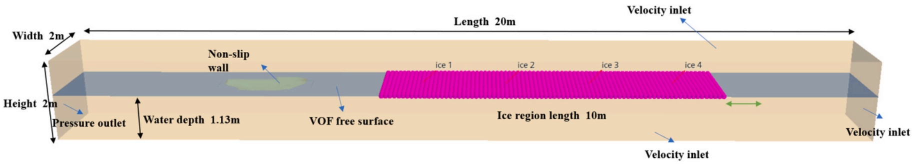

Fig. 9. The computational domain of numerical simulation.

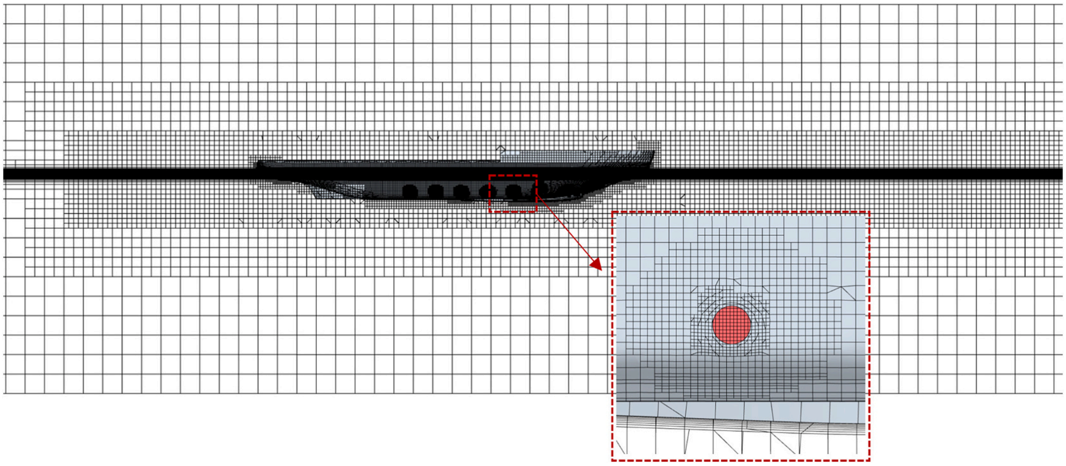

Fig. 10. Grid for numerical simulation.

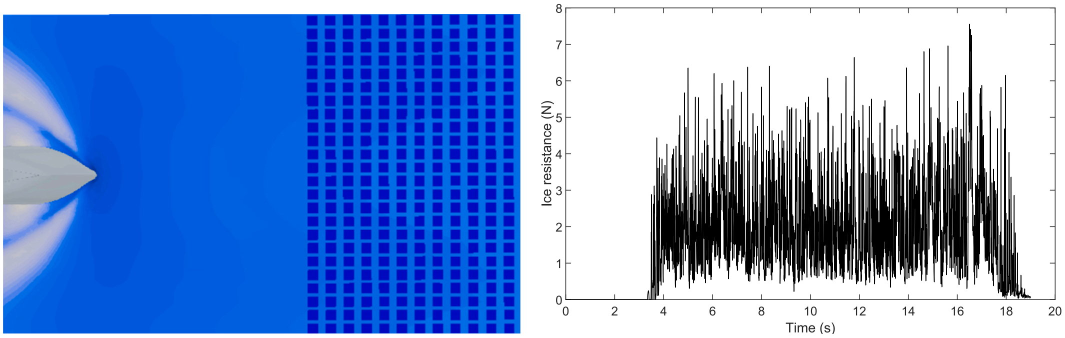

Fig. 11. The initial arrangement of the computational domain and the typical resistance time history curves of simulation.

included. The specific form of the governing equations is as follows (CD-Adapco, 2023):

$$\frac{\partial \rho}{\partial t} + \nabla \cdot (\rho \boldsymbol{v}) = 0 \tag{3}$$

$$\frac{\partial (\rho \boldsymbol{v})}{\partial t} + \nabla \cdot (\rho \boldsymbol{v} \otimes \boldsymbol{v}) = \nabla \cdot \boldsymbol{\sigma} + \boldsymbol{f}_b = \nabla \cdot (-p\boldsymbol{I} + \mathbf{T}) + \boldsymbol{f}_b \tag{4}$$

Where ρ represents fluid density, $\boldsymbol{v}$ denotes fluid velocity, $\otimes$ denotes the outer product, p stands for pressure, $\mathbf{f}_b$ is the resultant force acting on a unit volume of fluid, $\boldsymbol{\sigma}$ is the stress tensor, $\mathbf{I}$ denotes the identity tensor, and $\mathbf{T}$ represents the viscous stress tensor. The discretized continuity equation and momentum equation using the finite volume method are as follows:

$$\frac{\partial}{\partial t}\int_V \rho dV + \oint_A \rho \boldsymbol{v} \cdot \boldsymbol{da} = \int_V S_u dV \tag{5}$$

$$\frac{\partial}{\partial t}\int_V \rho \boldsymbol{v} dV + \oint_A \rho \boldsymbol{v} \otimes \boldsymbol{v} \cdot \boldsymbol{da} = -\oint_A p\boldsymbol{I} \cdot \boldsymbol{da} + \oint_A \boldsymbol{T} \cdot \boldsymbol{da} + \int_V \boldsymbol{f}_b dV + \int_V \boldsymbol{s}_u dV \tag{6}$$

Where t represents time, V denotes volume, a is the area vector, S_u and $\boldsymbol{s}_u$ are source terms.

In addition to the fluid phase, the solid discrete phase is treated with the DEM (Discrete Element Method), and its description follows the Lagrangian approach. The momentum change of particles is determined by the combined effects of surface forces and volume forces acting on them. The governing equations are based on Newton's second law, and the momentum and angular momentum equations are as follows:

$$m_p \frac{d\boldsymbol{v}_p}{dt} = \boldsymbol{F}_s + \boldsymbol{F}_b = \boldsymbol{F}_d + \boldsymbol{F}_p + \boldsymbol{F}_{vm} + \boldsymbol{F}_g + \boldsymbol{F}_c \tag{7}$$

$$\boldsymbol{I}_p \frac{d\omega_p}{dt} = \boldsymbol{M}_b + \boldsymbol{M}_c \tag{8}$$

In this equation, m_p is particle mass, $\boldsymbol{v}_p$ is particle velocity, $\mathbf{F}_s$ is surface force, $\mathbf{F}_b$ is body force, $\mathbf{F}_d$ is the drag force, $\mathbf{F}_p$ is pressure gradient force, $\mathbf{F}_{vm}$ is virtual mass force, $\mathbf{F}_g$ is the gravity, $\mathbf{F}_c$ is the contact force, $\mathbf{I}_p$ is the moment of inertia of the particle, ω_p is the angular velocity of the particle, $\mathbf{M}_b$ is the drag torque, $\mathbf{M}_c$ is the total moment from contact forces. The most crucial aspect lies in the calculation of drag forces and contact forces. The former involves the interaction between the fluid and solid phases, while the latter depends on the contact model chosen in the DEM method. The specific calculation methods for both will be further elaborated in subsequent sections.

In the numerical methodology employed in this study, the Volume of Fluids (VOF) method along with the High-Resolution Interface Capture (HRIC) scheme is utilized to capture the gas-liquid interface, simulating the presence of bubbles and free liquid surfaces. When employing the VOF method to capture the interface between immiscible fluids, it adheres to the assumption that the grid resolution is sufficient to solve for the position and shape of the interface between different phases. Therefore, in our numerical simulations, the shape and motion of subgrid scale bubbles cannot be described. The VOF method determines the position information of the interface by solving for the phase volume fraction α_i in each grid. Here, the subscript i denotes the ith phase, and α_i represents the proportion of the volume of the ith phase within the grid volume, with the stipulation that the sum of the volume fractions of all phases within each grid cell is equal to 1. Consequently, the material properties of each grid cell can be determined by using a weighted average method based on the volume fractions of each phase.

Once the VOF method is utilized to determine the interface and the material properties of the mixed fluids within each grid cell, the calculation of drag force $\mathbf{F}_d$ can be performed, with the equation as follows:

$$\boldsymbol{F}_d = 0.5C_d\rho_d\left(\frac{6\alpha_d}{4D}\right)\|\boldsymbol{v}_s\|\boldsymbol{v}_s \tag{9}$$

Where C_d is the drag coefficient, ρ_d is the density of the discrete phase, α_d is the volume fraction of the discrete phase, D is the characteristic diameter of the discrete phase, $\boldsymbol{v}_s$ is the relative velocity between the discrete phase and the continuous phase, and the determination of the drag coefficient is done through the Schiller-Naumann equation, with its specific form as follows::

$$C_d = \begin{cases} \dfrac{24}{Re_p}\left(1+\dfrac{1}{6}Re_p^{2/3}\right), & Re_p \leq 1000 \\ 0.424, & Re_p > 1000 \end{cases} \tag{10}$$

The definition of the particle Reynolds number is as follows:

$$Re_p = \frac{\rho_d\|\boldsymbol{v}_s\|D}{\overline{\mu}} \tag{11}$$

There $\overline{\mu}$ represents the dynamic viscosity of the multiphase mixture.

The calculation of contact force, $\mathbf{F}_c$, relies on the contact model within DEM, where the contact force equation in DEM represents a variant of the spring-damper model. The spring generates repulsive force to push particles apart, while the damper represents viscous damping, allowing for simulation of collision types beyond purely elastic ones. The force at the contact point is modeled as a pair of spring-damper oscillators. The parallel linear spring-damper model represents normal force, while tangential force (relative to the contact plane's normal vector) is represented by a series of parallel linear spring-damper units. In both cases, the spring accounts for the elastic response, whereas the damper considers energy dissipation during collisions. Illustrated for the two-dimensional case, the model is depicted in Fig. 12:

This paper employs the Hertz-Mindlin contact model to calculate the contact forces on discrete particles. The contact force between two DEM particles is determined by the following equation:

$$\boldsymbol{F}_c = F_n\boldsymbol{n} + F_t\boldsymbol{t} \tag{12}$$

Where F_n and F_t represent the magnitudes of the normal and tangential components, respectively, and $\boldsymbol{n}$ and $\boldsymbol{t}$ are the unit vectors in the normal and tangential directions, respectively. The normal vector is defined by the following terms:

The amplitude of the normal force:

$$F_n = -K_n d_n - N_n v_n \tag{13}$$

The normal spring stiffness is:

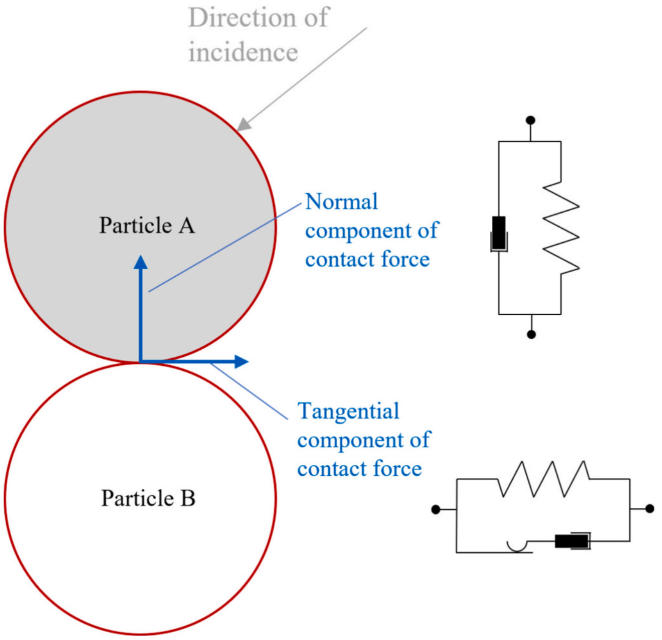

Fig. 12. Two-dimensional spring-damper model schematic.

$$K_n = \frac{4}{3}E_{eq}\sqrt{d_n R_{eq}} \tag{14}$$

The normal damping is:

$$N_n = \sqrt{5K_n M_{eq}}N_{n\ damp} \tag{15}$$

Where $N_{n\ damp}$ represents the normal damping coefficient, which is calculated by Eq. (19), and the tangential vector is defined by the following terms:

If $|K_t d_t| < |K_n d_n| C_{fs}$, where C_{fs} is the static friction coefficient, then the magnitude of the tangential force is calculated by $-K_t d_t - N_t v_t$, otherwise

$$F_t = \frac{|K_n d_n| C_{fs} d_t}{|d_t|} \tag{16}$$

The tangential spring stiffness is:

$$K_t = 8G_{eq}\sqrt{d_n R_{eq}} \tag{17}$$

The normal damping is:

$$N_t = \sqrt{5K_t M_{eq}}N_{t\ damp} \tag{18}$$

Where $N_{t\ damp}$ is the tangential damping coefficient, calculated by Eq. (20):

$$N_{n\ damp} = \frac{-ln(C_{n\ rest})}{\sqrt{\pi^2 + ln(C_{n\ rest})^2}} \tag{19}$$

$$N_{t\ damp} = \frac{-ln(C_{t\ rest})}{\sqrt{\pi^2 + ln(C_{t\ rest})^2}} \tag{20}$$

There，$C_{n\ rest}$ and $C_{n\ rest}$ are the artificially set normal and tangential restitution coefficient, and if $C_{n\ rest} = 0$ then $N_{n\ damp} = 1$, if $C_{t\ rest} = 0$ then $N_{t\ damp} = 1$.

In the above equations, R_{eq} stands for the equivalent radius, M_{eq} for the equivalent mass, E_{eq} for the equivalent Young's modulus, G_{eq} for the equivalent shear modulus, d_n and d_t represent the normal and tangential overlap distances at the particle contact point, respectively. When calculating the forces between particles and a wall, the above equations remain unchanged, assuming the radius and mass of the wall are infinitely large, hence the equivalent radius $R_{eq} = R_{particle}$ and the equivalent mass $M_{eq} = M_{particle}$.

4.2. Validation and analysis of numerical model results

In grid-based CFD numerical simulations, it is necessary to conduct grid convergence analysis to ensure numerical grid independence while maximizing computational efficiency. Four sets of grids were selected for validation, as shown in Table 4, with a ratio of $\sqrt{2}$ for the grid base sizes. Ice resistance was calculated under different grids to analyze the influence of grid size on accuracy.

As the basic grid size decreases, the number of grids increases and the ice resistance obtained from numerical calculations gradually converges, with an error of only 1.31 % between grid 3 and grid 4. The grids near the free surface directly determine the capture of the gas-liquid interface and play a decisive role in the data transfer between the DEM phase and the ship and fluid phases. When the grid is too large, it directly leads to the failure of collision detection of DEM particles with relatively high relative velocities, resulting in abnormally low ice resistance results for the ship. The convergence curve is shown in Fig. 13, and considering accuracy and computational efficiency, grid 3 is used for the numerical simulation in this study.

The numerical model was constructed entirely according to the experimental conditions. Therefore, experimental results were chosen to validate the numerical simulation. By comparing the numerical results with the experimental results for each condition, the rationality of the numerical model was examined. The comparison of resistance results between numerical simulation and experiments is shown in Fig. 14. It can be observed that the numerical simulation results are in good agreement with the experimental results, with overall errors within 10 %. Additionally, a comparison between the numerical results and experimental results of the open-water resistance before and after activating the air-bubbling system was made for a set of typical conditions (60 % ice concentration, 0.5 m/s velocity) to validate the accuracy of the numerical simulation for fluid modeling, as shown in Table 5. This validates the rationality of the numerical model established in this study.

Through numerical simulation, we can observe the process of the air-bubbling system more finely. As shown in Fig. 15(a), when the ship model begins to enter the ice floe area, the ice floe has not yet moved into the operational area of the air-bubbling system. At this point, the movement of ice floe is not affected by the air-bubbling system, showing a high degree of consistency between the two. As the vessel continues to navigate, as shown in Fig. 15(b), the air-bubbling system begins to affect the ice floe field, causing the ice floe to start detaching from the hull. When the vessel fully enters the ice floe area, as shown in Fig. 15(c), due to the continuous action of the air-bubbling system, the ice floe further detaches from the hull, resulting in a noticeable difference in the waterway behind the vessel. Specifically, the waterway behind the vessel widens significantly after the air-bubbling system is activated. Further observation of the movement of ice floe reveals that for vessels with the air-bubbling system activated, the ice floe area around the vessel can be divided into three parts: the first part is the area not covered by the air-bubbling system, which can be termed as the ineffective zone. It mainly refers to the bow position marked by the dashed box in Fig. 15(a), where the activation or deactivation of the air-bubbling system has no significant effect on the ice floe. The second part is the transitional zone, where the air-bubbling system begins to affect the movement of ice floe, but the ice floe has not completely detached from the hull. It is marked by the dashed box at the ship's shoulder position in Fig. 15(b). At this point, the gas-liquid mixed flow at the free surface begins to push the ice floe away from the hull, reducing the contact between the ship and the ice. The third part is the detachment zone, where the ice floe has completely detached from the hull, making it unable to exert resistance on the vessel. This is indicated by the dashed box in Fig. 15(c). Through the above analysis, we can further explain the factors affecting the efficiency of the air-bubbling system in Section 2 of this paper. Due to the existence of the first part of the ice floe area, even with an unlimited increase in gas flow rate, it is impossible to continuously reduce the ice resistance of the vessel, indicating that the increase in gas flow rate has a significant marginal effect. The increase in speed will slightly expand the proportion of ice floe in the first part of the area and elongate the second part, thereby affecting the efficiency of the air-bubbling system. The existence of the third part explains the phenomenon mentioned in Ni's work (2022), where maintaining a small gas flow rate on the side of the ship can ensure a good reduction in resistance efficiency for the air-bubbling system.

Table 4
Resistance values for different grid parameters.

Number	Basic size (m)	Number of grids	Ice resistance (N)	Error with the finest grid(%)
Grid 1	0.05	6.39×10^5	1.001	18.02
Grid 2	0.0354	1.24×10^6	1.166	4.50
Grid 3	0.025	2.49×10^6	1.205	1.31
Grid 4	0.0177	5.68×10^6	1.221	–

Through the above analysis, we can conclude that reducing the ineffective zone and transitional zone can effectively improve the ice resistance reduction effect of the air-bubbling system. This also provides a reference for the design of the air-bubbling system: we should place the first air nozzle toward the bow of the ship as much as possible and increase the gas flow rate of the front part of the shoulder while maintaining the total gas flow rate unchanged. For the nozzles in the detachment zone, only a small gas flow rate needs to be maintained.

This paper conducts the first comparative study between model ship experiments and numerical simulations of the air-bubbling system in ice floe. By comparing with the model ship experiments, the effectiveness of the numerical model of the air-bubbling system in ice floe is validated, and based on this, an analysis of the working principle of the air-bubbling system is conducted, and the operational areas of the system are defined.

4.3. Summary of empirical formulas for drag reduction rate of air-bubbling system

Through the comparison and verification in the previous sections, the numerical simulation method can accurately calculate the drag reduction of the air-bubbling system in ice floe channels. Through further analysis, we have delineated the functional areas of the air-bubbling system. To further investigate the factors affecting the drag reduction effect of the air-bubbling system, and ensure that the nozzle position of the air-bubbling system remains consistent with the previous ship model along the ship's length direction, we introduced two additional ship types for comparative analysis. The newly introduced ship types are the *KRISO container ship* (*KCS*) and *XUELONG 1* (*XL1*), which have a larger length-width ratio compared to the previous ship model. The focus of this study is to provide designers with a simple tool for a preliminary assessment of the drag reduction efficiency of the air-bubbling system during the conceptual design phase of ships. Therefore, we first consider the impact of basic ship parameters, such as length and breadth, on the drag reduction effect of the air-bubbling system. The shape of a ship is a highly complex three-dimensional curved surface, and it is not accurate enough to describe it using only basic parameters like length-to-breadth ratio. However, for the conceptual design phase of ships, the simple tool presented in this paper is effective. For more in-depth ship design phases, we hope to further investigate the influence of ship shape on the air-bubbling system in future research work. This paper first discusses the role of basic ship parameters.

The length-width ratios can be seen in Table 6. The comparison of the waterline profiles between the newly introduced ship models and the experimental ship model *XUELONG 2* (*XL2*) is shown in Fig. 16.

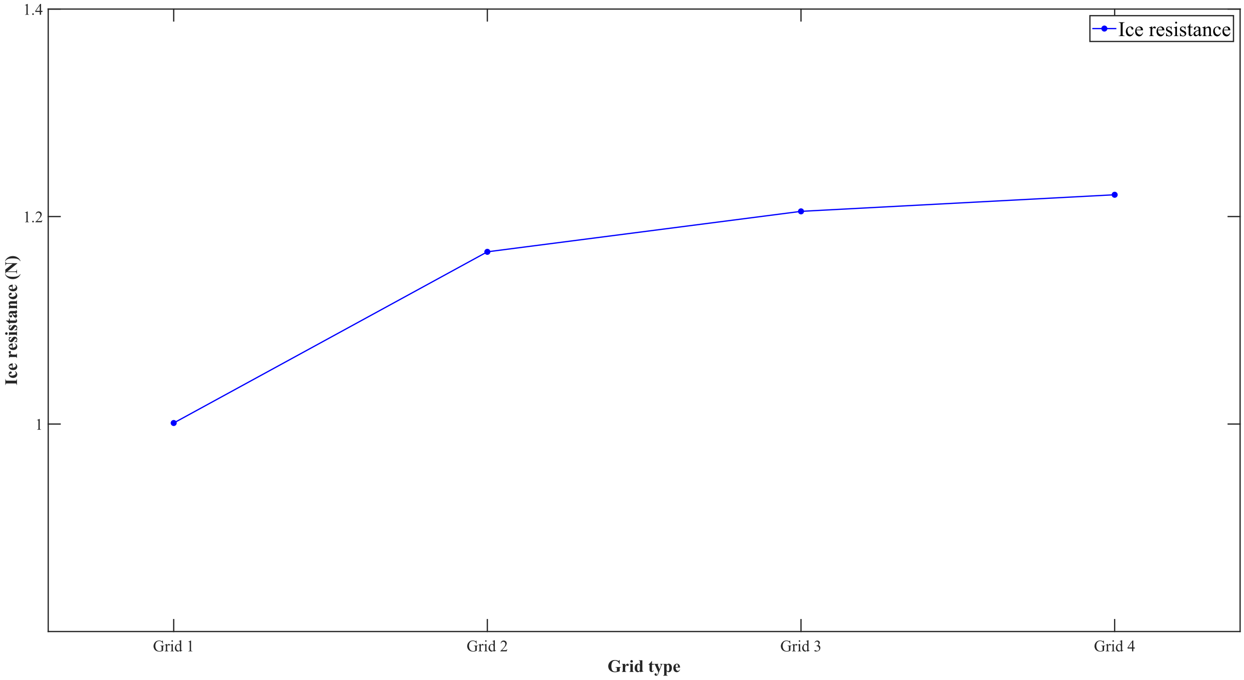

Fig. 13. Verification of grid size independence.

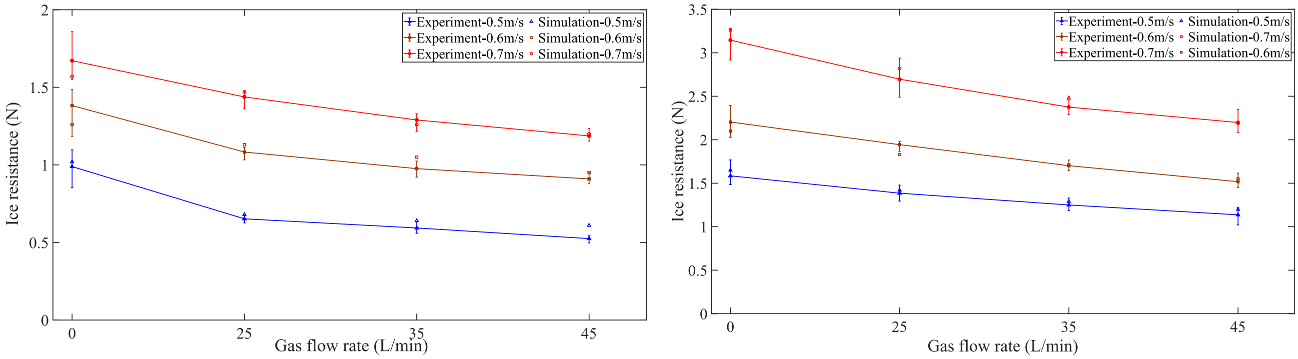

(a) 40% ice concentration

(b) 60% ice concentration

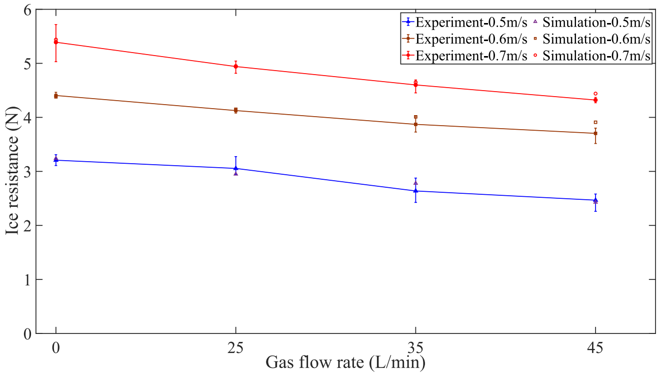

(c) 80% ice concentration

Fig. 14. Comparison of the numerical simulation and model test results.

Table 5
Comparison of open-water resistance.

	Air-bubbling system OFF	Air-bubbling system ON (25 L/min)	Air-bubbling system ON (45 L/min)
Experiment	0.535 N	0.566 N	0.570 N
Simulation	0.559 N	0.594 N	0.586 N

Table 6
Length-width ratios of different ship types.

Model name	L/B
XL2	5.262
XL1	6.858
KCS	7.341

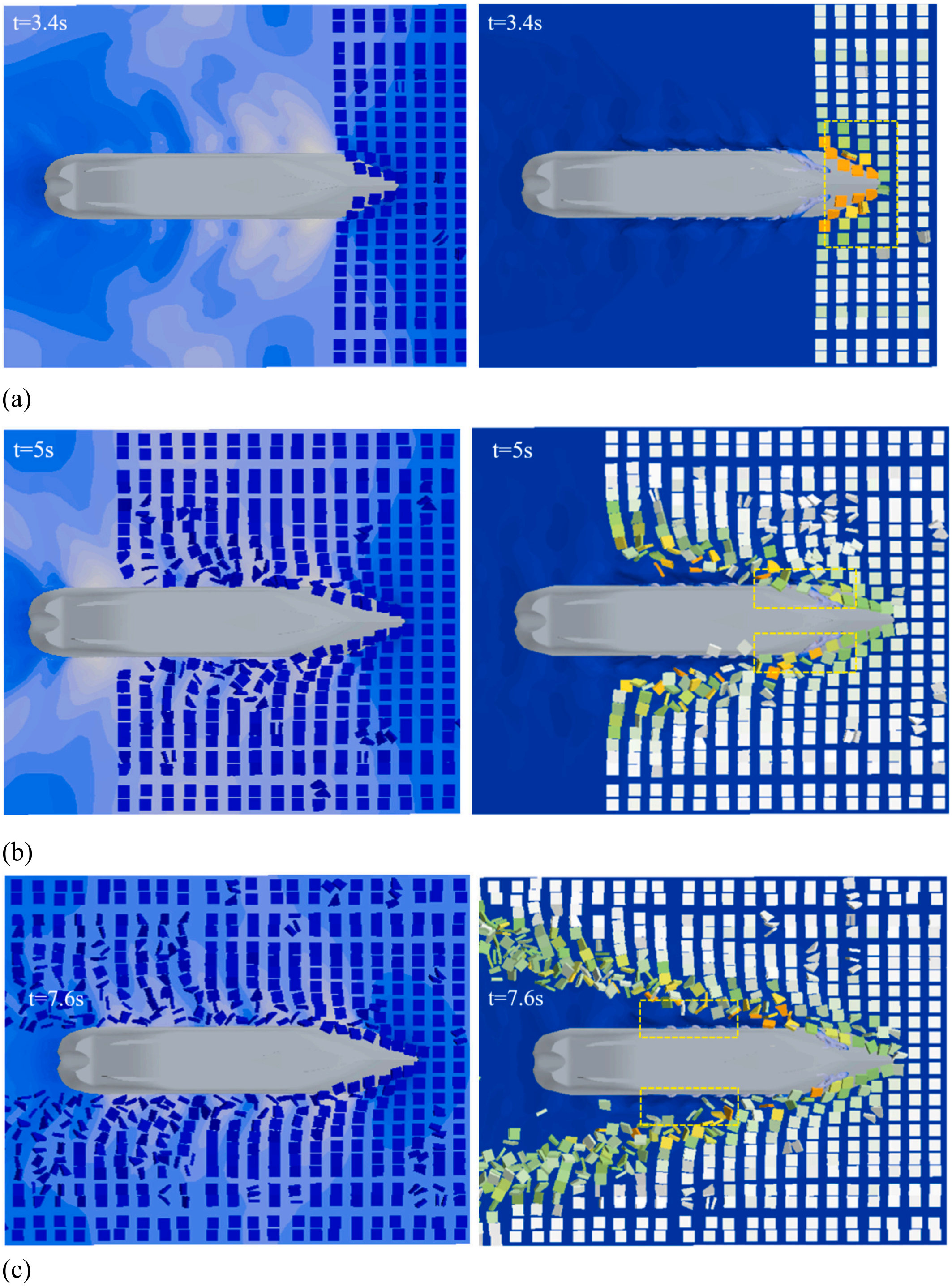

Fig. 15. Comparison of ice block movement before and after activating the air-bubbling system:(a) the bow begins to enter the ice floe region ; (b) the parallel middle body enters the ice floe region completely ; (c) the entire ship enters the ice floe region.

Fig. 16. Comparison of waterline shapes of different ship types.

Table 7
Matrix of conditions for new ship types.

Ship type	Ice concentration (%)	Towing speed (m/s)	Gas flow rate (L/min)
KCS/XL/XL2	40	0.6	0 25 45
KCS/XL/XL2	60	0.5	0 25 45
		0.6	0 25 45
		0.7	0 25 45
KCS/XL/XL2	80	0.6	0 25 45

For the newly introduced ship models, the simulation conditions are set based on a baseline condition of 60 % ice coverage and a sailing speed of 0.6 m/s. The settings are arranged in the form of an orthogonal matrix, with a total of 15 conditions for each ship type. The condition matrix is shown in Table 7.

Through numerical calculations, we can analyze the impact of the length-width ratio on the drag reduction effect of the air-bubbling system. By comprehensively comparing the drag reduction rate data of ship types with different length-width ratios, the results are shown in Fig. 17 below.

By observing the images, we can see that as the length-width ratio of the ship model increases, the drag reduction rate of the air-bubbling system also increases. This corresponds with the previous analysis of the functional areas of the air-bubbling system. An increased length-width ratio means the ship model is more slender, reducing the area of ineffective zones, and allowing the air-bubbling system to function more effectively. Further analysis of the air-bubbling system's effect on different ship models is shown in Fig. 18.

In Fig. 18, we can clearly observe the influence range of the ineffective zones of the air-bubbling system, as indicated by the yellow dashed outline. As the length-width ratio increases, the amount of ice in the ineffective zones decreases significantly. Consequently, the component of ice resistance that cannot be reduced by the jet system is reduced, thereby improving the drag reduction effect of the air-bubbling system. Further summarizing the variation of drag reduction rates of the bubble system with ship model length-to-width ratio under different ice coverage densities is shown in Fig. 19.

From the trend of drag reduction rate variation with increasing length-width ratio at 40 % and 80 % ice concentration in Fig. 18, it is observed that at 80 % ice concentration, a larger length-width ratio significantly enhances the drag reduction efficiency of the air-bubbling system.

Through extensive numerical calculations, a substantial amount of data on the drag reduction of the air-bubbling system has been obtained. While numerical simulations have significantly reduced costs compared to ship model tests, calculating the drag reduction rate of a new ship type using the air-bubbling system across various conditions still requires considerable time and resources. Therefore, this study aims to build upon existing data by employing basic linear fitting methods to derive an empirical formula for quickly estimating the drag reduction rate of the air-bubbling system. The formula, with drag reduction rate as the dependent variable and length-width ratio, ice concentration, Froude number, and gas flow rate as independent variables, can be obtained through linear fitting as follows:

$$\boldsymbol{R}_d = 100 \times \left(0.0226\frac{L}{B} - 0.1863C_i - 1.4314F_r + 0.005V_J + 0.1708\right) \tag{21}$$

Where $\boldsymbol{R}_d$ represents the drag reduction rate in percentage, L/B stands for length-width ratio (applicable range: 5.5–7.0), C_i denotes the ice concentration as a decimal (applicable range: 0.4–0.8), F_r refers to the Froude number (range: 0.11–0.16), and V_J (unit: L/min) is calculated by the following formula:

$$V_J = V_S \div \left(\frac{L}{2.04}\right)^{2.5} \tag{22}$$

Where V_S represents the gas flow rate of the ship's air bubbling system (unit: L/min).

The error of the linear fit is shown in Fig. 20, with fitting errors being less than 15 % except for a few specific conditions.

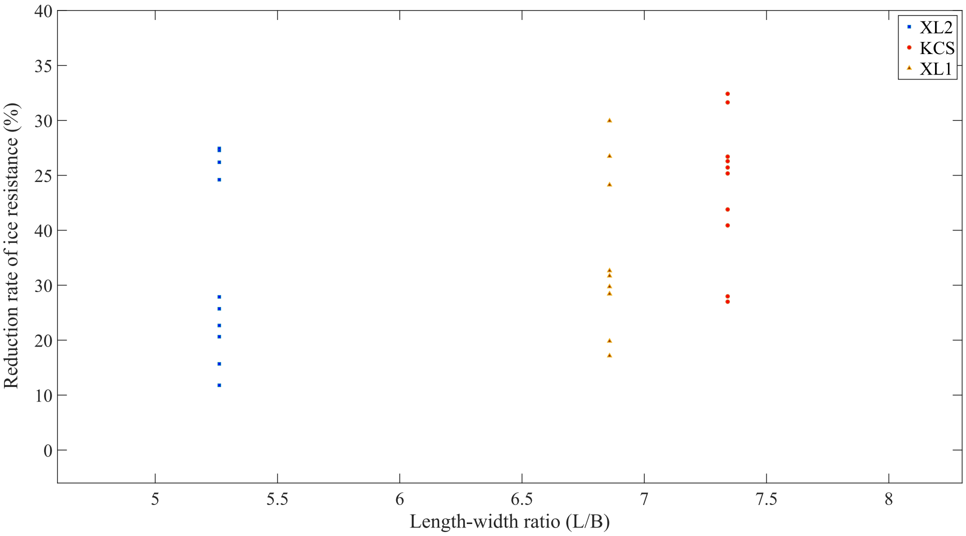

Fig. 17. Summary of drag reduction rates for different length-width ratios.

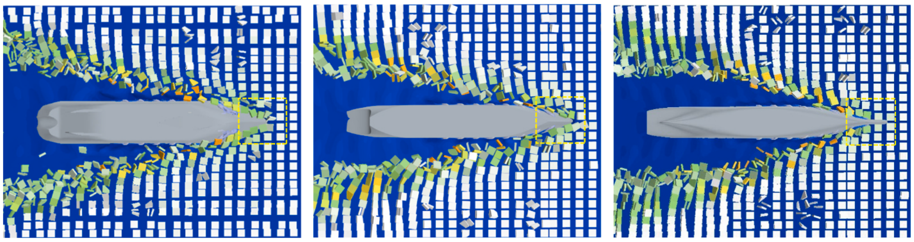

(a) the *XL2* (b) the *XL1* (c) the *KCS*

Fig. 18. Illustration of ineffective zones for different ship types.

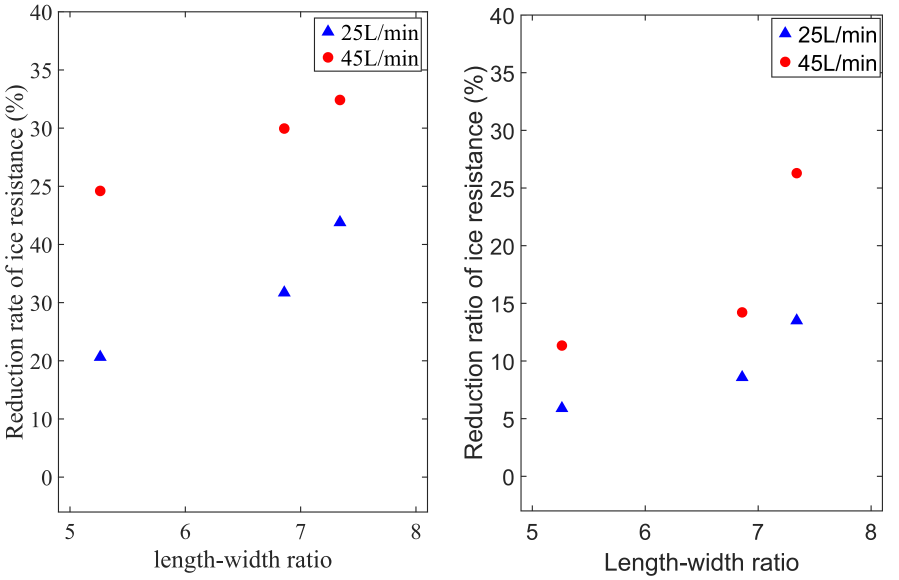

(a) 40% ice concentration (b) 80% ice concentration

Fig. 19. Illustration of drag reduction rate variation with length-width ratio at different ice concentrations.

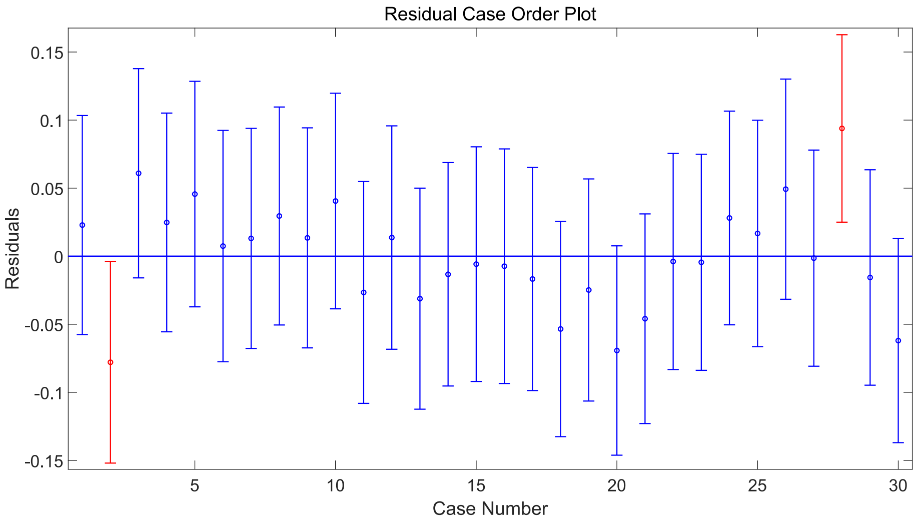

Fig. 20. Illustration of linear fit error.

In the ongoing research, the authors plan to further investigate the division of ice floe areas under the influence of different ice types and deployment patterns of the air-bubbling system using this numerical model. This will deepen our understanding of the design principles and optimization directions of the air-bubbling system, promoting the design of next-generation ice-capable vessel assistance systems.

5. Conclusion

This paper conducts analysis and research on factors affecting the ice resistance reduction effect of the air-bubbling system from the perspective of model ship scale through model ship experiments and numerical simulations. Through the experimentally validated numerical simulations, we can further explore the mechanism and influencing factors of the bubble system. This study focuses on the drag reduction effect of the air-bubbling system on three different ship types. Under the premise of consistent nozzle distribution, we conducted a numerical simulation to examine the impact of four factors—ship length-width ratio, gas flow rate, ship velocity, and ice concentration—on drag reduction. We believe that this fitting result can be used for preliminary estimation of the drag reduction effect of the air-bubbling system during the conceptual design phase of the ship, guiding further ship design. It should be noted that the impact of the bubble system is complex, and factors such as nozzle placement and ice conditions have a significant effect on the efficiency of the bubble system. This requires further research in the future. However, for the early design phase of a ship, the following conclusions can be drawn from this study:

1. Ice concentration is the most significant factor affecting the ice resistance reduction efficiency of the air-bubbling system. With increasing ice concentration, the efficiency of the air-bubbling system decreases significantly. This is because at high densities, ice around the ship is more likely to form large-scale force chains, making it difficult for the air-bubbling system to dislodge the ice around the ship in the gas-liquid mixed flow.
2. Speed has a more significant impact on the ice resistance reduction efficiency of the air-bubbling system at low densities, and this impact diminishes rapidly as ice concentration increases.
3. Increasing gas flow rate can effectively increase the ice resistance reduction efficiency of the air-bubbling system. However, as gas flow rate increases, there is a more pronounced marginal decrease. Especially for lower densities, the marginal decrease in efficiency becomes more significant as lower gas flow rates can significantly reduce ship-ice contact.
4. Through numerical simulation research, the area of the air-bubbling system's effect on ice around the ship is divided into ineffective zone, transition zone, and detachment zone, thus clarifying the design concept of the air-bubbling system.
5. By linearly fitting the drag reduction rate data obtained from existing numerical simulations, an empirical formula has been derived. This empirical formula can be used to quickly estimate the drag reduction rate of the air-bubbling system when applied to a new ship type.

CRediT authorship contribution statement

Hongyu Wei: Writing – original draft, Validation, Methodology, Investigation, Formal analysis, Data curation. **Baoyu Ni:** Writing – review & editing, Supervision, Resources, Project administration, Funding acquisition, Conceptualization. **Zhiyuan Li:** Writing – review & editing, Writing – original draft, Software, Formal analysis, Data curation, Conceptualization.

Declaration of competing interest

The authors declare that they have no competing financial interests or personal relationships that could have appeared to influence the work reported in this paper.

Acknowledgement

This work is supported by the National Natural Science Foundation of China (Nos. 52192693, 52192690, 52371270, U20A20327, 52350410468), the National Key Research and Development Program of China (2021YFC2803400), and the Natural Science Foundation of Heilongjiang Province (JJ2021TD0031), to which the authors are most grateful.

Data availability

Data will be made available on request.

References

Bergsma, J.M., Bouhuys, C.W., Schaap, T., et al., 2014. On the measurement of submersion ice resistance of ships, using artificial ice. In: The Twenty-fourth International Ocean and Polar Engineering Conference. Twenty-fourth International Ocean and Polar Engineering Conference, Busan, Korea, June 2014.

CD-Adapco, 2023. Simcenter STAR-CCM+ 2302 User Guide. Version 2302, Siemens, 2023. CD-adapco Inc., Melville, NY, USA. https://docs.sw.siemens.com/documentation/external/PL20221128664127487/userManual/starccmp_userguide_html/STARCCMP/index.html.

Corlett, E.C., Snaith, G.R., et al., 1964. Some aspect of icebreaker design. Trans. Royal Instit. Naval Architects 106 (4), 389–413.

Elbing, B.R., Mäkiharju, S., Wiggins, A., et al., 2013. On the scaling of air layer drag reduction. J. Fluid Mech. 2013 (717), 484–513.

Erland, M.S., Andrew, L.F., et al., 2012. Friction of ice on ice. J. Geophys. Res. Solid Earth 117 (B12).

Frederking, R., Barker, A., et al., 2002. Friction of sea ice on steel for condition of varying speeds. In: International Offshore and Polar Engineering Conference. Canadian Hydraulics Centre, National Research Council, Ottawa, Canada.

Guo, P.J., 2021. Experimental and Numerical Simulation Research on Resistance Reduction Mechanism of Air Bubble System. Harbin Engineering University.

Huang, Y., Huang, S.Y., Sun, J.Q., et al., 2018. Experiments on navigating resistance of an icebreaker in snow covered level ice. Cold Reg. Sci. Technol. 152, 1–14.

Juurmaa, K., et al., 1978. The Wärtsilä air-bubbling system. Polar Record 19 (119), 121–127.

Kim, M.C., Lim, T.W., Jo, J.C., et al., 2009. Comparison study on the propulsion performance for icebreaker with synthetic ice and refrigerated ice. J. Ocean Eng. Technol. 30 (1), 383–388.

Kim, E., Lu, W., Lubbad, R., et al., 2015. Toward a holistic load model for structures in broken ice. In: Proceedings of the 23rd International Conference on Port and Ocean Engineering under Arctic Conditions, Trondheim, Norway.

Lu, W., Lubbad, R., Løset, S., et al., 2016. Fracture of an ice floe: local out-of-plane flexural failures versus global in-plane splitting failure. Cold Reg. Sci. Technol. 2016 (123), 1–13.

McCormick, M.E., Bhattacharyya, R., et al., 2010. Drag reduction of a submersible hull by electrolysis. Nav. Eng. J. 85 (2), 11–16.

Ni, B.-Y., Chen, Z.W., Zhong, K., et al., 2020a. Numerical simulation of a polar ship moving in level ice based on a one-way coupling method. J. Marine Sci. Eng. 8 (9), 692.

Ni, B.-Y., Guo, P.J., Xue, Y.Z., et al., 2020b. Experimental study of the mechanism of an air-bubbling system in a small ice water tank. J. Harbin Eng. Univ. 41 (6), 777–783.

Ni, B.-Y., Zhong, K., et al., 2021. An experimental study on the reduction of collision between a ship and crushing ice by using an air-bubbling system. J. Vibr. Shock 40 (4), 10–16.

Ni, B.-Y., Wei, H.Y., Li, Z.Y., et al., 2022. Numerical simulation of an air-bubble system for ice resistance reduction. Journal of Marine Science and Engineering 10 (9), 1201.

Sodhi, D.S., et al., 1995. Northern Sea route reconnaissance study: a summary of icebreaking technology. DIANE Publ. 95 (17), 1995.

Song, W.C., Wang, C., Wei, Y.J., et al., 2019. Experimental research on drag reduction characteristics of underwater vehicle during pitching. Acta Armamentarii 40 (9), 1902–1910.

Timco, G.W., et al., 1984. Ice forces on structures: physical modeling techniques. Second IAHR State Art Report Ice Forces Struct. Hamburg, Germany 1984 (4), 117–150.

Timco, G.W., Weeks, W.F., et al., 2010. A review of the engineering properties of sea ice. Cold Reg. Sci. Technol. 60 (2), 107–129.

Vroegrijk, E., et al., 2015. Validation of CFD+ DEM against measured data. In: International Conference on Offshore Mechanics and Arctic Engineering. American Society of Mechanical Engineers, Newfoundland, Canada. May 31–June 5, 2015.

Wang, J.M., Jiang, M.S., et al., 2004. Study of drag reduction of vessel model by microbubble with different injection forms in the towing basin. J. Huazhong Univ. Sci. Technol. 32 (12), 78–80.

Wang, L.Y., Hao, S.W., et al., 2011. On the development of bubble drag reduction technique. Ship Ocean Eng. 40 (6), 109–113.

Wilkman, G., et al., 2011. Experience of air-bubbling system in ice navigation and future possibilities. In: OTC Arctic Technology Conference, Houston, Texas, USA.

Woolgar, R.C., Colbourne, D.B., et al., 2010. Effects of hull–ice friction coefficient on predictions of pack ice forces for moored offshore vessels. Ocean Eng. 37 (2–3), 296–303.

Yang, B.Y., Sun, Z., Zhang, G.Y., et al., 2024. Non-smooth discrete element method analysis of channel width's effect on ice resistance in broken ice field. Ocean Eng. 2024 (313), 119419.

Zhong, K., Ni, B.-Y., Li, Z.Y., et al., 2023. Direct measurements and CFD simulations on ice-induced hull pressure of a ship in ice floe fields. Ocean Eng. 2023 (272), 113523.

Zong, Z., Yang, B.Y., Sun, Z., et al., 2020. Experimental study of ship resistance in artificial ice floes. Cold Reg. Sci. Technol. 2020 (176), 103102.